Effects of heat-producing elements on the stability of deep mantle thermochemical piles

R.I. Citron[1], D.L. Lourenço[2], A.J. Wilson[3], A.G. Grima[3], S.A. Wipperfurth[4], M.L Rudolph[2], S. Cottaar[5], L. Montesi[4]

[1]Department of Earth and Planetary Science, University of California, Berkeley
[2]Department of Earth and Planetary Sciences, University of California, Davis
[3]Department of Earth Sciences, University College London
[4]Department of Geology, University of Maryland, College Park
[5]Department of Earth Sciences, University of Cambridge

Key Points:

- Thermochemical piles can be stable even if they are enriched in heat-producing elements
- Piles could constitute a primordial/enriched mantle reservoir
- Seismic properties of enriched piles may be consistent with large low velocity provinces (LLSVPs)

Corresponding author: Robert Citron, `ricitron@gmail.com`

Abstract

Geochemical observations of ocean island and mid-ocean ridge basalts suggest that heat producing element (HPE: U, Th, K) abundances vary within the mantle. Combined with bulk silicate Earth (BSE) models and constraints on the Earth's heat budget, these observations suggest the presence of a more enriched (potentially deep and undepleted) reservoir in the mantle. Such a reservoir may be related to seismically observed deep mantle structures known as Large Low Shear Velocity Provinces (LLSVPs). LLSVPs might represent thermochemical piles of an intrinsically denser composition, and many studies have shown such piles to remain stable over 100s of Myr or longer. However, few studies have examined if thermochemical piles can remain stable if they are enriched in HPEs, a necessary condition for them to constitute an enriched HPE reservoir. We conduct a suite of mantle convection simulations to examine the effect of HPE enrichment up to 25x the ambient mantle on pile stability. Model results are evaluated against present-day pile morphology, and tested for resulting seismic signatures using self-consistent potential pile compositions. We find that stable piles can form from an initial basal layer of dense material even if the layer is enriched in HPEs, depending on the density of the layer and degree of HPE enrichment, with denser basal layers requiring increased HPE enrichment to form pile-like morphology instead of a stable layer. Thermochemical piles or LLSVPs may therefore constitute an enriched reservoir in the deep mantle.

Plain Language Summary

The amount and distribution of radioactive heat-producing elements within the mantle exerts an important control on the thermal evolution of the mantle and core. Determining the composition of the mantle and its rate of heat production is difficult because several lines of evidence suggest that the Earth's mantle is not homogeneous, containing reservoirs of unmixed material. Such reservoirs may contain material enriched in radioactive elements, and could be primordial, remaining isolated from the surface since Earth's formation. One possible physical location for such a reservoir is within 'piles' of compositionally distinct material in the deep mantle. Such piles have been suggested by seismic observations, but it is unclear whether piles can persist if they are enriched in radioactive elements that heat the piles, promoting their buoyant rise and entrainment into the convecting mantle. We use geodynamic models to explore the dynamics of a compositionally-distinct basal layer enriched in heat-producing radioactive elements. We determine the conditions under which the layer can be organized into piles that remain stable over geological timescales. We find that piles can remain stable, and we are able to reconcile the dynamical requirements for stability with seismic observations using models of lower mantle physical properties.

1 Introduction

The bulk composition of the Earth's mantle, particularly the amount and distribution of radioactive heat producing elements (HPEs) U, Th, and K is still uncertain. One of the main constraints on the amount of HPEs in the Earth is the observed surface heat flux of 46 $\pm$ 3 TW (Jaupart et al., 2015), generated by an uncertain combination of radiogenic heat (from HPEs in the crust and mantle) and primordial heat (from planetary accretion and core formation). The HPE abundance in the crust, accounting for $\sim$40% of the Earth's radiogenic heat production, is well constrained by analysis of exposed crust and xenoliths (Rudnick & Gao, 2014). Bounds on the concentration of HPE within the mantle are less certain, with estimates primarily based on the comparison of meteorites with the solar composition and constraints based on the generation of MORB and OIB from mantle melting (McDonough & Sun, 1995; Arevalo et al., 2013). Assuming a 20 TW bulk silicate earth (BSE) (McDonough & Sun, 1995) and an estimated 8 TW of heat produced by HPEs in the lithosphere (Huang et al., 2013), the convecting mantle is left with 12 TW from radiogenic heat production. A MORB source composition (G-MORB DMM Model: Arevalo et al., 2013) applied to the bulk

convecting mantle yields only 7 TW of radiogenic heat, suggesting another reservoir of HPEs that produces the remainder of heat (in this case 5 TW). Whether or not such a reservoir exists and how enriched in HPEs it may be depends on the assumed BSE composition and the reservoir's mass. As an extreme case, low-heat producing BSE models (e.g., Javoy et al., 2010; O'Neill & Palme, 2008) do not require a hidden reservoir. However, an enriched mantle reservoir is also supported by geochemical and geochronological observations of OIBs. OIB lavas exhibit significantly higher $^{3}He/^{4}He$ and lower $^{40}Ar/^{39}Ar$ ratios relative to MORB, and are comparatively more heterogeneous, pointing to a variety of sources, some of which have not been significantly mixed with the MORB source mantle and are less degassed and more enriched in HPEs (Kellogg & Wasserburg, 1990; Hofmann, 1997; Arevalo et al., 2013; Deschamps et al., 2015; White, 2015). Arevalo et al. (2013) estimates the OIB source comprises 19% of the mantle by mass. Such findings suggest that HPE abundances vary within the mantle, and may require a (potentially deep) mantle reservoir enriched in HPEs (Kellogg, 1992). If such a reservoir is spatially located within the Large Low Shear Velocity Provinces (LLSVPs), which comprise approximately 9% of the mantle by mass (Cottaar & Lekic, 2016), the present-day heat production within the reservoir could be $\sim$ 10-100 times higher than the ambient mantle. Even more enrichment in HPEs would be required if the LLSVPs are only $\sim$2% of the mantle by mass (e.g., Burke et al., 2008; Hernlund & Houser, 2008). Such enrichment could possibly cause the reservoir to heat up over time and become gravitationally unstable. We report here on the long-term stability of HPE-enriched reservoirs in the lower mantle.

Understanding the nature and stability of a mantle reservoir enriched in HPEs, and its connection to seismic heterogeneity, is critical to understanding the bulk composition of the mantle and its evolution and dynamics over time. It is possible that an enriched reservoir is related to observed or hypothetical deep mantle structures, such as LLSVPs, Ultra Low Velocity Zones (ULVZs), viscous blobs, or strong silica enriched mid-mantle structures (e.g., G. F. Davies, 1984; Becker et al., 1999; Kellogg et al., 1999; Ballmer, Houser, et al., 2017). Perhaps the most promising enriched reservoir consists of deep thermochemical piles of dense material with higher concentrations of HPEs. Observations of LLSVPs suggest the existence of such structures in the deep mantle, and numerical mantle convection simulations show that dense thermochemical piles (henceforth, piles) can be stable over geological timescales (e.g., M. Li et al., 2014). Plumes sourced from the edges and tops of such piles could entrain enriched pile material, explaining the undegassed component observed in OIB sources. Dense piles in the lowermost mantle could be composed of either primordial material or recycled oceanic crust (Deschamps et al., 2011), both of which may create piles enriched in HPEs. Primordial material could result from either compositional layering during magma ocean solidification (e.g. Labrosse et al., 2007; Deschamps et al., 2012) or subducted Hadean crust (e.g., Tolstikhin et al., 2006), and studies of noble gases from deep mantle sources have shown that lower mantle heterogeneity has been stable and isolated since the first 100 Myr of Earth history (Pető et al., 2013; Mukhopadhyay, 2012). Recent examination of kimberlites also suggest an isolated primordial reservoir that has persisted since at least 2.5 Ga (Woodhead et al., 2019). Alternatively, recycled oceanic crust leftover from decomposed subducted slabs could also form LLSVPs (Hofmann, 1997; U. Christensen & Hofmann, 1994; Coltice & Ricard, 1999; Tackley, 2011; Mulyukova et al., 2015). Piles could also be composed of a mix of both primordial material and recycled basalt, and entrainment of such a reservoir into mantle plumes could explain the variety of the geochemical and geochronological observations associated with hot spot volcanism (Ballmer et al., 2016). Regardless of the origin of pile material, geological and geophysical evidence indicates that LLSVPs have been stable as two separate piles for at least the last 200 Myrs (D. R. Davies et al., 2015; Buffett, 2014; Conrad et al., 2013; Dziewonski et al., 2010).

In a convecting mantle where density differences arise due to both temperature variations and intrinsic density variations, diverse convective regimes can develop, leading to stratified convection, isolated piles, or complete entrainment and mixing of contrasting ma-

terials (e.g., Deschamps & Tackley, 2008, 2009). If LLSVPs are thermochemical piles, they must remain dynamically stable. We use 'stability' here to refer to the ability of piles of dense material to exist as a distinct and persistent reservoir for 100s of Myr without being entrained into the mantle or reverting to a layer of basal material. Alternatively, if the pile material is thought to be primordial then pile stability can also be defined as the ability of piles to persist over the age of the Earth. Previous studies (e.g., Tackley, 1998; Davaille, 1999; Montague & Kellogg, 2000; Le Bars & Davaille, 2004; McNamara & Zhong, 2004; Mulyukova et al., 2015; M. Li et al., 2018) have explored the range of conditions under which piles form from an initial basal layer of high density material, and subsequently can remain stable over geological times. In general, stability is mostly controlled by the buoyancy number, which describes the ratio of chemical to thermal contributions to density anomalies of the material. Piles have been found to be stable for buoyancy numbers of 0.6-0.8, under different geometries and under different thermal contrasts across ambient mantle and pile material (e.g., M. Li & McNamara, 2018; McNamara & Van Keken, 2000). McNamara and Zhong (2005) and N. Zhang et al. (2010) have taken this a step further and shown that by integrating modern plate velocities into mantle convection simulations, it is possible to reproduce the present-day LLSVP morphology as observed in seismic tomography.

However, despite the large amount of previous work on pile stability, few studies have examined if piles enriched in HPEs are dynamically stable, a critical need in determining the viability of LLSVPs as an enriched mantle reservoir. Kellogg et al. (1999) demonstrated that a basal layer enriched in HPEs could form stable piles, however, this basal layer is only enriched by a factor of 5 and has a thickness of 1600 km, which is too thick given more recent constraints on LLSVP volume (e.g., Cottaar & Lekic, 2016). van Thienen et al. (2005) examined various magnitudes of HPE enrichment in a basal layer, and found that HPE enrichment could have a strong effect on layer stability, resulting in stable piles for various HPE enrichment values and basal layer densities. In contrast, Deschamps and Tackley (2008) state that HPE enrichment of a basal layer only has a small effect on its stability. McNamara and Zhong (2004) and M. Li and McNamara (2018) also found that the inclusion of HPE enrichment in a basal layer had a limited effect on the long-term evolution of the mantle, however both studies only conducted a single simulation with an HPE enriched basal layer (by a factor of 5 or 10, respectively) as part of a larger suite of (non-HPE-enriched) pile stability simulations. van Summeren et al. (2009) also conducted a single simulation with a basal layer enriched by a factor of 10, and found that it decreased layer stability. Thus, while numerical simulations (e.g., Kellogg et al., 1999; van Thienen et al., 2005) and experimental work (Limare et al., 2019) have shown that piles enriched in HPEs could be stable, the magnitude of enrichment at which piles of varying density are stable remains unresolved.

It is also unclear if piles enriched in HPEs are compatible with the seismic properties of LLSVPs inferred from seismic tomography. Seismic tomographic models also show general agreement in the predicted boundaries of LLSVPs near the core-mantle boundary (Lekic et al., 2012; Cottaar & Lekic, 2016), with estimates for CMB-coverage across six tomographic models ranging from 24 to 28% (Cottaar & Lekic, 2016). The heights and volumes of LLSVPs are less constrained. Estimates of the sizes of LLSVPs based on shear wave tomographic models range from 2% (Burke et al., 2008) to 9% of the total mantle mass (Cottaar & Lekic, 2016), but elevated temperatures on top of piles could mask the boundaries in shear wave velocity and lead to overestimation of their size (Ballmer, Lourenço, et al., 2017). Tomographic modeling places mean S-wave residuals in the LLSVPs at around -2-3% (e.g., Koelemeijer et al., 2015; Moulik & Ekström, 2016; French & Romanowicz, n.d.) while higher frequency body waves map the lateral boundaries of the LLSVPs to show a 3-5% shear wave velocity drop (e.g., Ni & Helmberger, 2003; To et al., 2005; Wang & Wen, 2007; Lay & Garnero, 2011). LLSVPs are less well constrained and pronounced in P-wave tomographic models. The ratio of $\mathrm{d}lnV_S$ to $\mathrm{d}lnV_P$ ranges on the order of 1.5 to 5 (e.g., Koelemeijer et al., 2015), but results can vary based on choices made in the tomographic modeling procedure (Tesoniero et al., 2016). The density of LLSVPs is also unclear, with

evidence for LLSVPs being denser (e.g., Moulik & Ekström, 2016; Lau et al., 2017) or lighter (e.g., Koelemeijer et al., 2017) than the surrounding deep mantle. These inferred seismic properties of LLSVPs can be used to constrain which geodynamically modeled piles may represent viable LLSVP analogs (e.g., Kellogg et al., 1999).

In this work, we use 2D numerical models of mantle convection to understand the effects of HPE enrichment in a dense layer (or piles), and whether HPE-enriched material can persist as an isolated reservoir over the age of the Earth. We examine how pile formation and stability depends on the initial basal layer density and HPE enrichment. We find that stable piles can form from dense basal layers enriched in HPEs, which confirms the possibility that a reservoir of HPEs in the mantle could be associated with the LLSVPs. Enrichment in HPEs increases the maximum compositional density contrast at which piles can form, allowing denser basal layers to form stable piles. However, too much HPE enrichment in less dense basal layers can result in total entrainment. For models that produce pile-like behavior at the present day, we explore if the chosen buoyancy ratio and the resulting temperature of the piles can produce seismic signatures that are consistent with observations of LLSVPs.

2 Methods

2.1 Mantle convection models

We simulate convection in the Earth's mantle using the finite element code ASPECT version 2.0.1 (Heister et al., 2017; Kronbichler et al., 2012; Bangerth et al., 2018a, 2018b; Gassmöller et al., 2016), built on deal.II version 9.0.1 (Alzetta et al., 2018). We conduct 2D simulations of thermochemical convection in a rectangular box using the Boussinesq approximation, solving the governing equations for conservation of mass, momentum, and energy:

$$\nabla \cdot \mathbf{u} = 0, \tag{1}$$

$$-\nabla \cdot [\eta(\nabla \mathbf{u} + \nabla^T \mathbf{u})] + \nabla P' = (\rho - \rho_0) g \mathbf{e_z}, \tag{2}$$

$$\rho_0 C_p (\frac{\partial T}{\partial t} + \mathbf{u} \cdot \nabla T) = \nabla \cdot k \nabla T + \rho_0 H, \tag{3}$$

where $\mathbf{u}$ is the velocity, η is the viscosity, P' is the dynamic pressure, ρ is the density, ρ_0 is the reference density of ambient mantle, g is the gravitational acceleration, T is the temperature, C_p is the specific heat at constant pressure, k is the thermal conductivity, H is the heating rate per unit mass, and $\mathbf{e_z}$ is the unit vector in the z direction (normal to the surface).

We adopt a set of parameters that is representative of Earth-like convective vigor, heat production, and a simplified form of the depth-dependence of viscosity. The viscosity is temperature dependent and is given by,

$$\eta(z, T) = \eta_0(z) \exp\left(-A \frac{T - T_{\text{ref}}}{T_{\text{ref}}}\right), \tag{4}$$

where T_{ref} is the reference temperature and η_0 is the reference viscosity, which is 6.15×10^{22} Pa·s for the lower mantle (<670 km) but is decreased by a factor of 30 above 670 km to approximate a less viscous upper mantle. The thermal viscosity exponent A is set to 4.8, to allow viscosity to vary due to temperature by approximately four orders of magnitude. With these parameters, the Rayleigh number, $Ra = \frac{\rho \alpha g (T_1 - T_0) D^3}{\kappa \eta_0}$, at the start of the simulation is $\sim 3.34 \times 10^5$ for the lower mantle. We provide a complete list of parameters and their values in Table 1.

Each simulation begins with a basal layer of higher density material in the lower 150 or 300 km of the mantle. The density difference between the basal layer and ambient mantle is characterized by the buoyancy number, $B = \Delta\rho/\alpha\rho_0(T_1 - T_0)$, where $\Delta\rho$ is the density difference between high-density basal layer material and the ambient mantle, and α is the coefficient of thermal expansion. Density therefore varies due to both thermal expansion and composition, so that $\rho = (\rho_0 + \Delta\rho C)\alpha(T - T_{\text{ref}})$, where C is the composition value of the cell (1 = pure high density basal layer material, 0 = pure ambient mantle). Changes in composition are tracked using tracer particles that are advected with the fluid flow (Gassmöller et al., 2016, 2019). Each cell's composition value is based on the average composition of the advected particles in the cell.

Each simulation is run in a 2890 km × 8670 km domain with a fixed resolution of 256 × 768 cells. For load balancing, tracer particles are created and destroyed over the course of each simulation so that at each timestep a cell has a minimum of 60 or maximum of 80 tracer particles. Doubling the resolution or number of tracer particles for a few select test cases did not affect the large-scale dynamics, and was beyond our computational limitations to do for all simulations. The initial temperature of each simulation is 1600 K throughout the mantle, with a high frequency sinusoidal temperature perturbation (50 wavelengths across the width of the domain, in order to avoid imposing any initial structure) that has a maximum amplitude of 30 K at the mid-mantle but decreases as a cosine function towards the top and bottom of the domain, so that $T(x, z) = T_{\text{ref}} + 30\sin(\pi z/h)\sin(50 \cdot 2\pi x/w)$, where w and h are the width and height of the box, respectively (Figure 1a). We also initialize the simulations with small thermal boundary layers at the top and bottom of the domain, which are given by a conductive cooling or heating profile (error function) for a timescale of 5 Myr (so that at least a few cells are part of the initial thermal boundary layer). We use periodic side boundary conditions and free-slip top and bottom boundary conditions. We also subtract the net x-translation mode in order to maintain a stationary reference frame while using free-slip top and bottom boundaries.

We conduct a suite of simulations considering both constant heating and radioactive decay, over a range of different buoyancy numbers. For cases with constant heating, the ambient mantle heating rate is 6.039×10^{-9} W m^{-3}, which reflects the combination of isotopic heating rates and ambient mantle concentrations required to approximate the present-day heating rate of the mantle as calculated from a compilation of MORB samples and an assumed 10% partial melting (G-MORB DMM Model of Arevalo et al., 2013). For cases with radioactive decay (henceforth, decay heating), we consider the time-dependent heat production of the HPEs given in Table 2, where the heating rate of the initial ambient mantle (at 4.5 Gyr) is calculated by propagating the abundances of HPEs from Arevalo et al. (2013) back through time. In both constant and decay heating cases, the heating rate in the basal layer is given a value of 1, 5, 10, 15, 20, and 25 times the heating rate in the ambient mantle. The volumetric heating rate over time for the decay heating model is shown in Figure S1 in Supplementary Information. Overall, we examine two basal layer thicknesses (150 or 300 km), two types of heating (constant or decay), six factors of HPE enrichment in the basal layer relative to the ambient mantle (1, 5, 10, 15, 20, 25), and four buoyancy numbers (0.4, 0.6, 0.8, 1.0), corresponding to an intrinsic density difference between high-density basal layer material and the ambient mantle $\Delta\rho$ of 39−99 kg m^{-3} or 1.2−3 %, for a total of 96 simulations. Recall that the buoyancy number is defined such that a higher B means a higher density contrast and a lower B means a lower density contrast. Each simulation is run for 4.5 Gyr.

3 Results

An example of a typical simulation outcome that resulted in a stable pile is shown in Figure 1. In this simulation, strong convection initiates at $\sim$ 1.35 Gyr with a large initial overturn of the basal layer into a large pile with a central peak (Figure 1b). For the remainder of the simulation, the pile remained present but changed shape over time,

Table 1: Model physical parameters.

Parameter	Symbol	Value
Mantle thickness	D	2890 km
Ambient mantle density	ρ_0	3300 kg m^{-3}
Top temperature	T_0	300 K
Bottom temperature	T_1	3300 K
Reference temperature	T_{ref}	1600 K
Reference viscosity	η_0	6.15×10^{22}, 2.05×10^{21} Pa·s
Specific heat	C_p	1250 J K^{-1} kg^{-1}
Thermal conductivity	k	4.7 W m^{-1} K^{-1}
Thermal expansivity	α	1×10^{-5} K^{-1}
Gravitational acceleration	g	9.8 m s^{-2}

Table 2: Model chemical parameters: HPE nuclide heating rate per mass of nuclide (h), half-life ($t_{1/2}$), and concentrations in the ambient mantle at present (AM) and at 4.5 Gyr (AM_i). Radiogenic heating parameters for each of the nuclides are from Ruedas (2017).

Nuclide	h (W/kg)	$t_{1/2}$ (Gyr)	AM (ppb)	AM_i (ppb)
^{238}U	9.4946×10^{-5}	4.468	8.2	17
^{235}U	5.6840×10^{-4}	0.704	0.059	5.0
^{232}Th	2.6368×10^{-5}	14.0	24	30
^{40}K	2.8761×10^{-5}	1.248	13	160

sometimes briefly splitting into two piles that later merged back together. As seen in Figure 1, even over the last 500 Myr there were large changes in pile morphology; however, the bulk convective regime generally stabilized in the last 500-1000 Myr of each simulation.

We classified the outcome of each simulation into three regimes: layered convection, piles, and entrainment (Figure 2). For layered convection (Figure 2a), the basal layer remained spread over the entire bottom of the domain. While the layer did contain some topography, there was negligible CMB exposure. This highlights the usefulness of CMB exposure in identifying morphological regimes, compared to other LLSVP observables such as the aspect ratio of the piles and the slope of the pile interface topography. In the piles regime (Figure 2b,c), a stable pile (or several piles) formed and remained stable throughout the later stages of the simulation. Piles generally covered ∼20-80% of the CMB, and were bounded by portions of the CMB that were directly exposed to the ambient mantle (e.g., Figure 2b,c). Pile morphology, such as the height and number of piles, varied depending on B and HPE enrichment. In general, higher values for B and more HPE enrichment lead to higher piles (from the CMB) and more piles (never more than three). In the entrainment regime (Figure 2d), the basal layer became nearly completely entrained and mixed into the ambient mantle over time. While piles may have formed initially, they decreased in size over the course of the simulation, so in the late stages of the simulation they covered a marginal fraction of the CMB.

For the four main cases for our simulations (either constant or decay heating, with an initial basal layer thickness of 150 or 300 km), we classified each simulation into one of the three regimes defined above (Figure 3). We distinguished stable pile formation from layered convection and total entrainment based on the CMB exposure (the fraction of the simulation

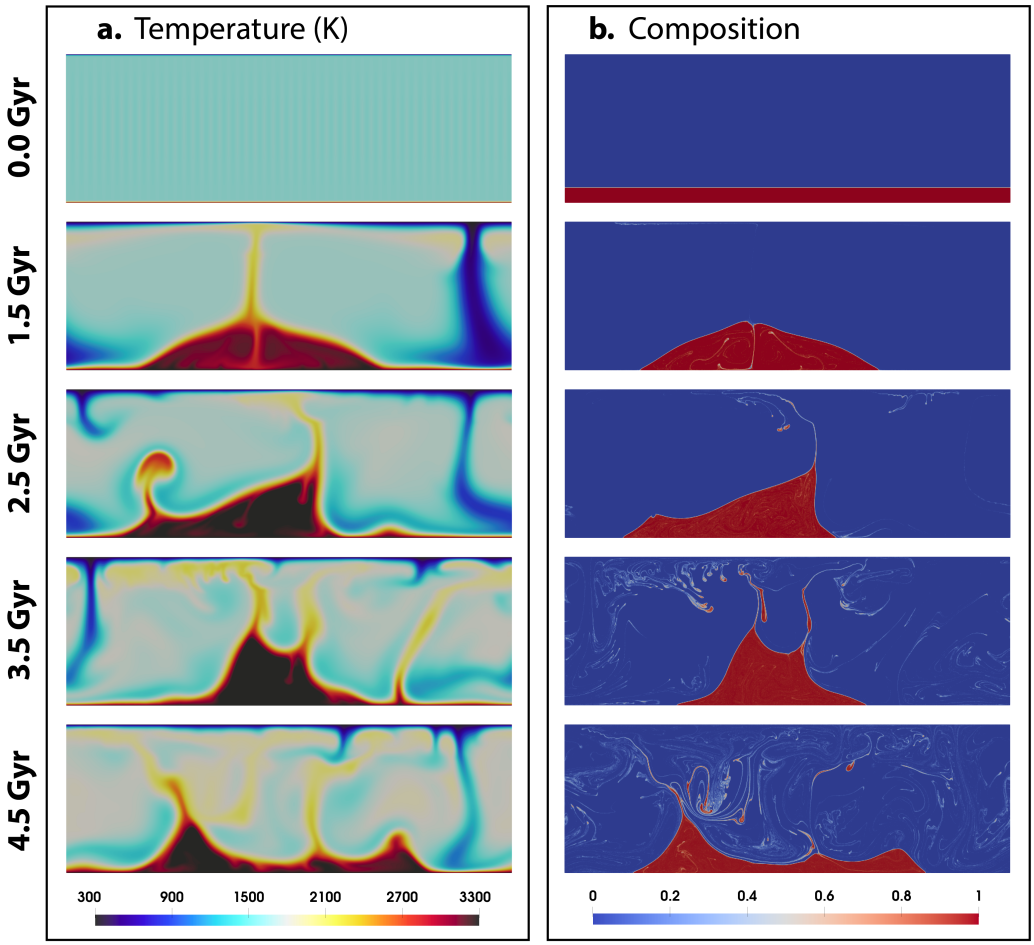

Figure 1: Evolution of (a) temperature and (b) composition for a simulation with constant heating, h = 300 km, $B = 0.6$, and 10x HPE enrichment. The composition is 1 for basal layer material and 0 for ambient mantle. Vigorous convection begins at $\sim$ 1.35 Gyr with an initial overturn in the basal layer. A pile forms and remains stable over the last 1 Gyr, with varying morphology over time. Two additional cases, with identical parameters except for either an initial basal layer thickness of 150 km or an HPE enrichment of 25x, are shown in Figures S2 and S3, respectively, in Supplementary Information.

lower boundary not covered by pile material), an often used quantity for describing pile formation (e.g., M. Li & McNamara, 2018). The CMB exposure tracked well with other metrics of pile stability, such as aspect ratio and perimeter length, but ultimately gave a more consistent and continuous trend with our dataset. In order to capture the bulk end state of each simulation, we averaged the CMB coverage over the last 500 Myr of the simulation. Examining only the last timestep may only capture transient behavior (as seen in Figure 1, because pile morphology could change over 10s of Myr timescales). We classified a simulation as having stable piles if the average fractional CMB coverage over the last 500 Myr was between 0.2 and 0.8. Below 0.2 we classified the simulation as layered convection, and above 0.8 we classified the outcome as entrainment. Although there actually is a continuous spectrum of pile stability and these boundaries are somewhat arbitrarily defined, this scheme seemed to generally capture the pile stability observed through visual analysis of the system behavior. Simulations with average CMB exposures of 0.2-0.8 over the last 500

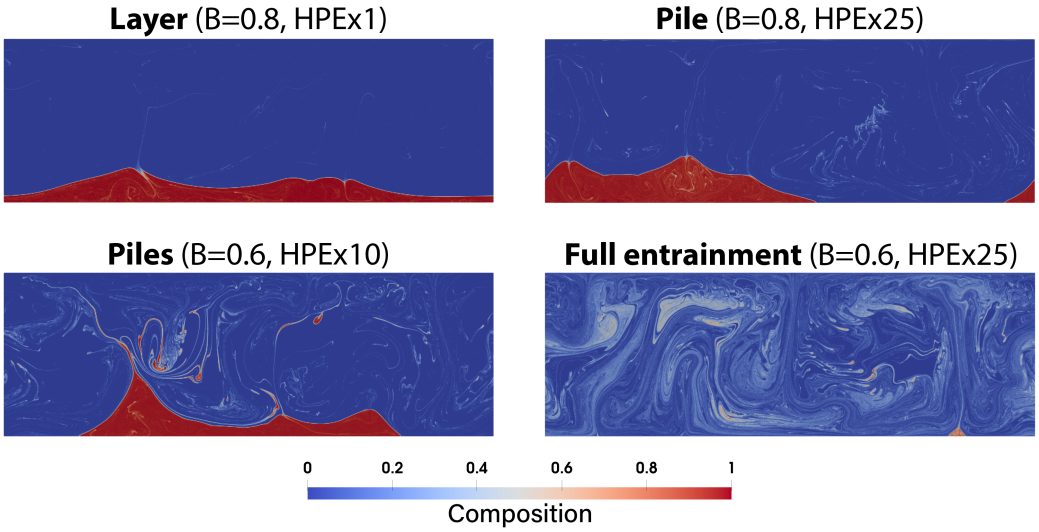

Figure 2: Example of model outcomes, showing the last timestep (4.5 Gyr) for simulations with an initial basal layer thickness of 300 km, and which outcomes are (top left) layered convection, obtained for higher B and less HPE enrichment, (top right and bottom left) pile or piles, obtained for higher HPE enrichment or lower B, and (bottom right) full entrainment, obtained with low B and high HPE enrichment. The composition is 1 for basal layer material and 0 for ambient mantle. Outcomes for cases with an initial basal layer thickness of 150 km are shown in Figure S4 in Supplementary Information.

Myr contained pile-like structures sufficiently discrete to be surrounded by regions of CMB directly exposed to the ambient mantle, and with topography extending above the original height of the basal layer. In Figure 3 we report both the classification and the percent CMB coverage for each simulation. We again note that the transition between regimes is more continuous than shown in our regime diagram (Figure 3), and our classification into distinct regimes is more for clarity in interpreting the results of our simulation; slightly different boundaries between regimes could shift the regime diagram, but the general trends will be preserved. We investigated adjusting the regime classification bounds and found that the overall trends are preserved within reasonable limits.

We found that it was possible to form stable piles from a basal layer that was enriched in HPEs, but the stability of piles strongly depended on the amount of HPE enrichment and B of the basal layer (Figure 2). In general, piles formed at intermediate values of B, with less HPE enrichment required for lower B (0.6) and more HPE enrichment required at higher B (0.8). Layered convection typically occurred at higher B and lower HPE enrichment, and entrainment occurred at lower B and higher HPE enrichment. Piles were formed in similar regimes in both the constant heating and decay heating cases, but CMB exposure was generally greater in decay heating cases. Increased CMB exposure may be due to either increased entrainment resulting in smaller piles, or the piles becoming taller and narrower. Piles were also easier to form for the thinner 150 km thick basal layer than in the 300 km thick layer.

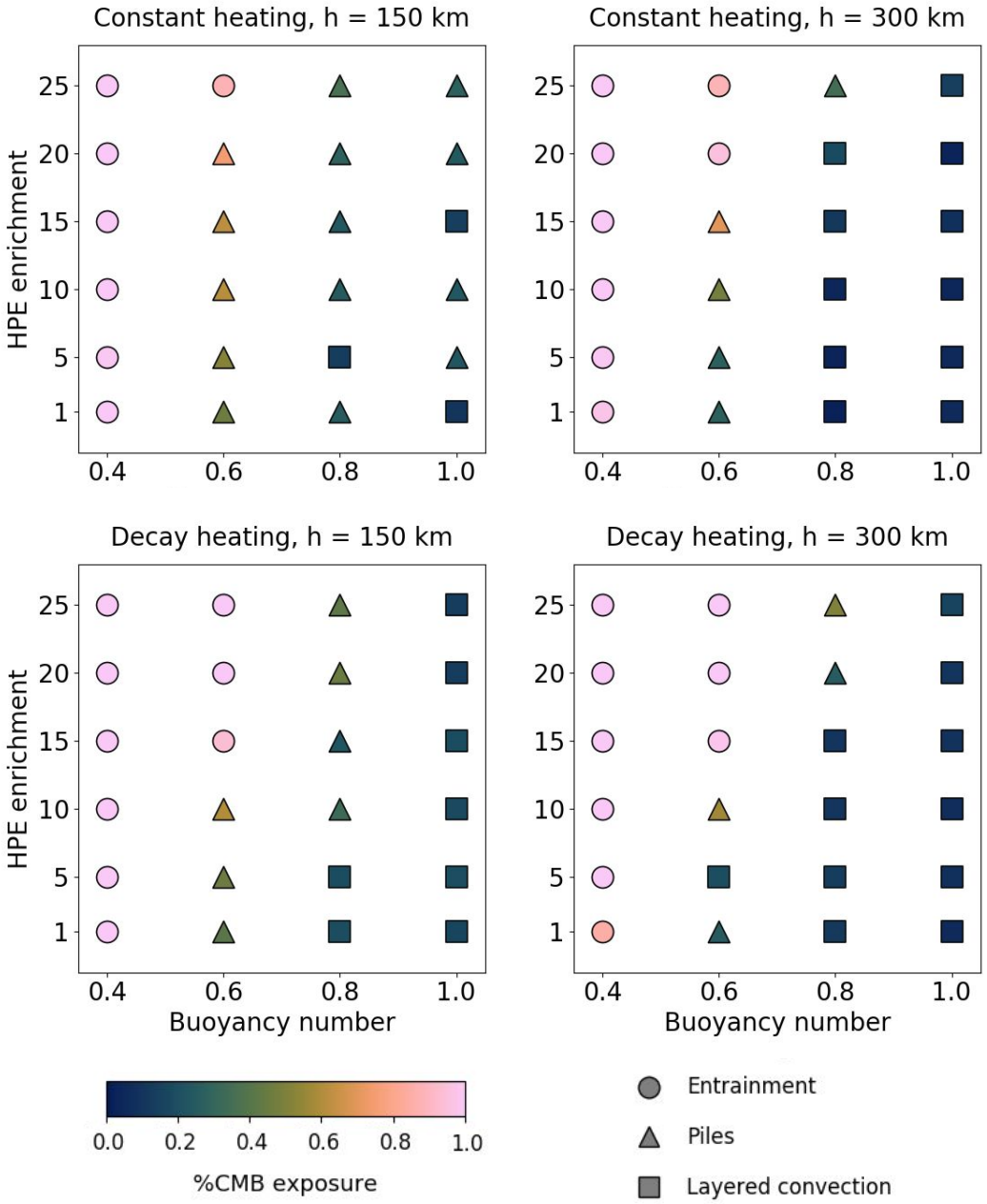

Figure 3: Regime Diagram for constant heating (top panels) and decay heating (lower panels) using initial pile thickness of 150 km (left panels) and 300 km (right panels). HPE enrichment is the factor of increase of HPE concentration in the initial basal layer relative to the ambient mantle. Entrainment (circle), piles (triangle), and layered convection (square) are classified by core mantle boundary (CMB) exposure of >0.8, 0.2−0.8, and <0.2, respectively, where CMB exposure of 1.0 is 100% exposure. Note that the regime transitions are progressive but are made discrete here for clarity.

4 Discussion

4.1 HPE enrichment and BSE constraints

Our results imply that piles in the deep mantle, similar to LLSVPs, can remain stable even if they are enriched in HPEs by a factor of 1 to 25 relative to the ambient mantle (Figure

3). While the exact HPE enrichment that produces stable piles could change depending on model geometry and other simplifying assumptions (see Section 4.4), our results can be used to identify general trends in how pile stability depends on HPE enrichment, and provide insight on how HPE enrichment in a hidden reservoir of deep mantle piles can constrain BSE models. Compared to other studies that examined pile stability in unenriched piles, we find that the inclusion of HPE enrichment in the piles can affect the range of acceptable intrinsic density differences between the piles and the ambient mantle. For example, at higher B, HPE enrichment can allow pile formation from basal layers normally too dense to produce piles (Figure 3). At lower B, too much HPE enrichment can result in total entrainment instead of stable piles. In general, our results are consistent with those of van Thienen et al. (2005), Kellogg et al. (1999), and Limare et al. (2019), which also find that stable HPE enriched piles can persist as a distinct mantle reservoir over geologic time scales.

The amount of HPEs that can exist in piles without disrupting pile stability bounds the allowable contribution of a hidden reservoir of LLSVP-like piles to the global BSE heat budget. The total heat production for the BSE is 20 $\pm$ 4 TW for the medium heat production models of McDonough and Sun (1995) and Palme and O'Neill (2014), 11 $\pm$ 2 TW for low heat production models (Javoy, 1999; Javoy et al., 2010; O'Neill & Palme, 2008), and 33 $\pm$ 3 TW for high heat production models (Turcotte & Schubert, 2014) (see Šrámek et al. (2013) for overview of BSE models). The contribution to BSE heat production from a hidden reservoir of piles depends on the HPE enrichment factor and volume of pile material. The LLSVPs are an estimated 9% of the mantle by mass (Cottaar & Lekic, 2016), in between the $\sim$5 or 10 % mantle by mass the 150 and 300 km in our simulations represent, respectively. The enriched heating rates of the layers would yield 6.1 TW (14.8 TW) in the 150 km (300 km) layer for an HPE enrichment factor of 25, and 1.3 TW (3 TW) in the 150 km (300 km) layer for an HPE enrichment factor of 5, when considering the necessary volume adjustment for the spherical Earth. The 150 km case is consistent with the medium heat production model, while the 300 km case is consistent with the medium and high heat production models. It should be noted that these calculations would overestimate the heat production from the piles if the composition of the ambient mantle is more depleted than the G-MORB composition we assume, for example, the N-MORB composition from Arevalo et al. (2013). We should also note that ULVZs can be potentially enriched in HPEs as well (e.g., Labrosse et al., 2007), which could imply less HPE enrichment in LLSVPs. However, ULVZs are a much lower volume compared to LLSVPs (e.g., McNamara, 2019) and therefore could not constitute as much of a contribution to the BSE heat budget.

The stability of enriched piles in our simulations suggests that plumes sourced from LLSVPs could sample a reservoir enriched in HPEs. OIB isotopic data also indicates that at most 10-30% of OIB material should come from a degassed source that may reside inside piles or LLSVPS (Deschamps et al., 2011). Similar to previous work (McNamara, 2019, and references therein), our simulations show plumes originating from the topmost boundary of the piles, which could provide a pathway for the entrainment of material from the pile to the surface. McNamara (2019, and references therein) suggest that entrainment has to be confined to the root of the plume, limiting the mixing between the dense and chemically distinct material of the pile from that of the surrounding mantle. While piles could be composed of primordial material and/or recycled oceanic crust, by examining both constant and decay heating over 4.5 Gyr, we show that enriched piles can persist as a stable reservoir over geological timescales regardless of their origin.

4.2 Thermal evolution

The present day heat-flow of the Earth is sustained by a combination of secular cooling of the mantle and core, inner core solidification, and radiogenic heat production in the crust and mantle. The thermal evolution of the mantle is influenced by the extent and duration of CMB coverage by thermochemical piles. In the layered convection regime, extensive CMB coverage insulates the core and reduces heat flow across the CMB (M. Li

& McNamara, 2018; Nakagawa & Tackley, 2004), resulting in a cooler background mantle (e.g., Kellogg, 1997) and decreasing the density contrast between the basal material and the background mantle. Introducing convective layering reduces the convective vigor through the dependence of convective vigor (Ra) on layer thickness. If convective vigor decreases, the basal layer can heat up, promoting a transition from layered convection to pile formation, steep pile morphology, and more entrainment (M. Li & McNamara, 2018). In the fully entrained regime, near total CMB exposure (the absence of piles and/or a basal layer), leads to secular cooling which results in mantle temperatures that decrease monotonically through time (U. R. Christensen, 1985; McNamara & Van Keken, 2000). Alternatively, stable piles represent an intermediary regime between full CMB exposure and coverage. Gradual changes in pile morphology translate to gradual changes in the CMB heat-flux to the ambient mantle. This implies that the presence of piles discourages catastrophic initial cooling of both core and mantle. Pile morphology can therefore exert a primary control on the cooling rate of the mantle over time. The effect of HPE enrichment on the ability of piles to regulate the thermal evolution of the mantle is unclear based on conflicting results from prior studies (Kellogg et al., 1999; McNamara & Zhong, 2004; M. Li & McNamara, 2018).

Our results indicate that HPE enrichment can strongly influence pile morphology and CMB exposure, affecting the long-term thermal evolution of the mantle. Figure 4 illustrates the effect of HPEs at different enrichments (10 and 25 times that of the ambient mantle compared to no enrichment) for constant and decay heating cases, on CMB exposure, CMB heat-flux, surface heat flux and mantle temperature over time (Figure 4). In general, after piles start to form the mantle temperature increases as there is more CMB exposure, and correspondingly more heat flux from the core into the ambient mantle. The initial dramatic change observed for all plots in Figure 4 after the first $\sim$1 Gyr is symptomatic of our models' initial perturbation and overturn event and is reflected in the CMB coverage, average mantle temperature and root mean square velocity plots (Figure 4 a-d).

Figure 4 indicates that trends in CMB exposure over time for both constant and decay heating (Figure 4a) mimic the CMB and surface heat-flux trends (Figure 4b). The models with the highest HPE enrichement exhibit the highest percentage of CMB exposure and the highest values of CMB and surface heat flow. These runs also exhibit the fastest velocities (Figure 4d) and the highest average mantle temperature (Figure 4c). For simulations with HPE enrichment of 25 times more than the ambient mantle and B less than 0.8, we note that by the end of the simulation all pile material has been entrained and assimilated into the mantle. We also note that these high HPE concentrations lead to increasing average mantle temperatures over time, in excess of 2500 K. In contrast, simulations with no relative enrichment favor layered convection and therefore full CMB coverage. Similar to previous work (M. Li & McNamara, 2018; McNamara & Zhong, 2004) these models favor a cooler average mantle temperature that decreases with time. Alternatively, in models with moderate HPE concentrations, piles form and remain stable over time. These simulations exhibit relatively stable CMB exposure, average mantle temperatures, and CMB and surface flux over the last 1 Gyr of simulation time or more (see orange line in Figure 4a-c). This behaviour is in agreement with results from M. Li and McNamara (2018), who also observe increasing upper mantle temperatures with increasing CMB exposure. This indicates that pile stability is associated with near constant mantle temperatures and can thus act as a marker or better still a thermostat for mantle temperatures.

It is important to note however, that the dimensional average temperatures plotted in Figure 4 do not include the mantle adiabat which increases average mantle temperatures by ~ 500 k. Moreover, we also neglect core cooling and implement an initial mantle temperature condition that is cooler than that estimated for the Archean Earth. Although previous studies indicate that the initial mantle temperature has little to no effect on the present day surface temperature and the thermal evolution of core and mantle (Nakagawa & Tackley, 2014, 2004; M. Li & McNamara, 2018), a higher initial mantle temperature could affect the

time at which piles form due to the lower mantle viscosity and increased initial vigor of convection. Higher initial temperatures should be tested in future work to provide better constraints on the relationship between HPE enrichment, pile stability, and the thermal evolution of our planet.

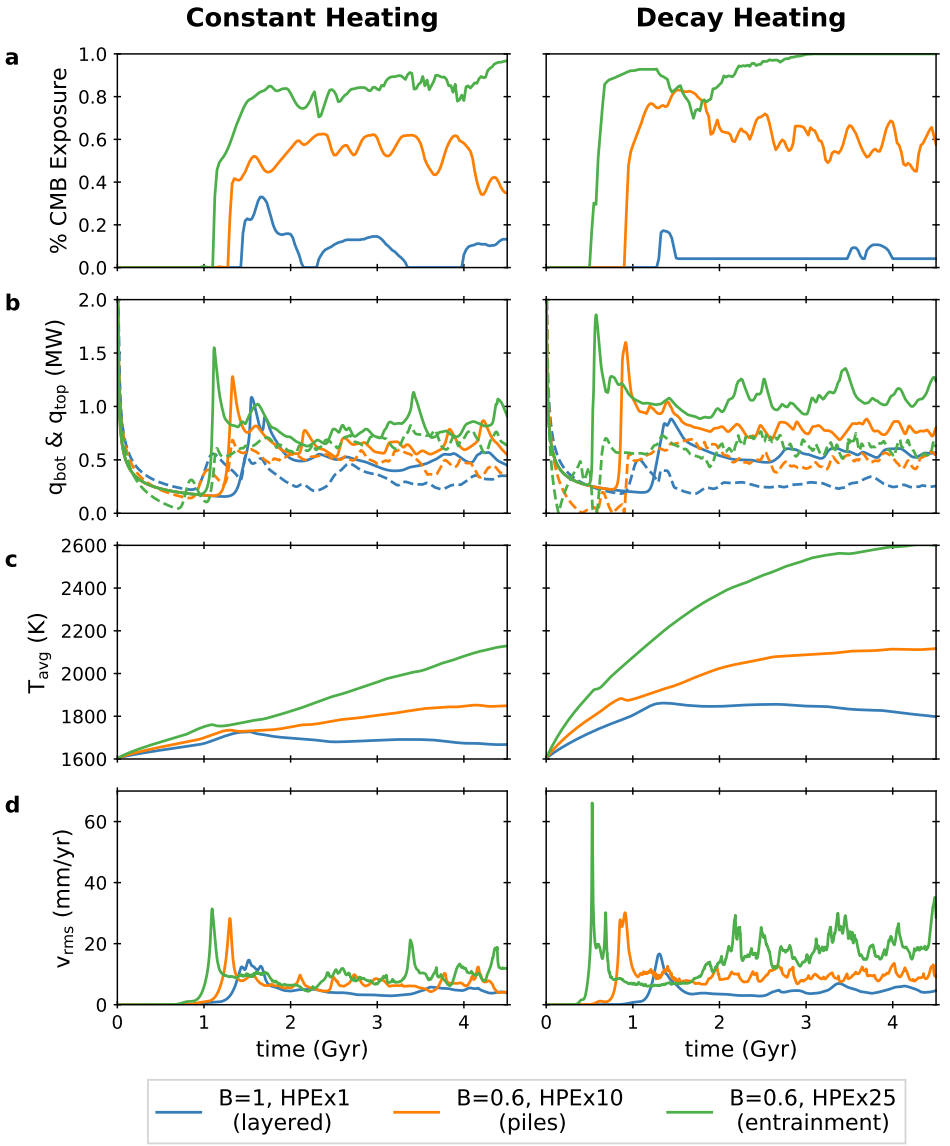

Figure 4: Evolution of select example simulations over time (present day at 4.5 Gyr), showing (a) percent CMB exposure, (b) heat flow through the bottom (dashed lines) and top (solid lines) of the model domain, (c) average mantle temperature, and (d) RMS velocity. An example simulation that results in each of layered convection (B=1, HPEx1), piles (B=0.6, HPEx10), or entrainment (B=0.6, HPEx25) is shown for both constant radiogenic heating (left column) and radiogenic heating with decay (right column).

4.3 Seismic constraints

Our geodynamic models place constraints on the range of intrinsic density differences that can produce chemical piles, but a comparison between the geodynamic models and tomographic models requires additional models for the relationship between seismic wavespeeds, composition, temperature, and density. The composition of the piles could represent basal structures enriched in iron resulting from the middle out crystallization of a magma ocean in early Earth history (Labrosse et al., 2007) or the subduction of slabs to the core mantle boundary (Deschamps et al., 2011). Iron enrichment increases density and results in reduced shear velocities in dominant mantle phases (e.g., Jackson et al., 2006; Mao et al., 2008), and has been shown to satisfy commonly agreed upon seismic signatures of LLSVPs (e.g., Garnero & McNamara, 2008; McNamara & Zhong, 2005). Some seismic observables are sensitive to density variations, which permits the development of models of lowermost mantle density heterogeneity (e.g., Ishii & Tromp, 2001; Moulik & Ekström, 2016). Efforts to infer density variations are complicated by observational and theoretical challenges including the dependence of model results on starting structure (Kuo & Romanowicz, 2002) and a lack of sensitivity to odd-degree structure (Resovsky & Ritzwoller, 1995). At present, there is a lack of consensus among groups developing models using different data constraints and theoretical frameworks for the inversions. Improved measurements of the splitting of ${}_0S_2$ have enabled refined models of lowermost mantle density (Deuss et al., 2011, 2013). A joint inversion for density and wavespeeds constrained by normal mode splitting, travel times, and waveform data prefers a model with ∼0.5-0.6% density excess associated with the lowermost ∼500 km of the LLSVPs (Moulik & Ekström, 2016). Constraints from modeling the tidal response of the solid earth also favor a density excess within the LLSVPs of ∼ 1.5%, confined to the lowermost 150 km (Lau et al., 2017). The splitting of Stoneley modes, a class of normal modes with sensitivity near the CMB, is most compatible with LLSVPs that have net buoyancy relative to the ambient mantle but cannot constrain the sign of the buoyancy in the bottom ∼100 km of the LLSVPs (Koelemeijer et al., 2017). Thus, while recent models of lowermost mantle density variations differ somewhat in the pattern, magnitude and depth distribution of variation of density variations, all of the existing models may be compatible with a scenario in which the bottom ∼ 100 km of the LLSVPs have 0.5-1.5% excess density but that the LLSVPs as a whole may be close to neutrally buoyant.

In order to test if the stable piles produced in our simulations could be consistent with the inferred seismic properties of LLSVPs, we computed the expected seismic properties of the piles in our simulations for a range of plausible compositions, the details of which are described in the Supplementary Information. We use the BurnMan thermo-elastic code (Cottaar et al., 2014) combined with the database from Stixrude and Lithgow-Bertelloni (2011) to calculate the range of potential pile compositions which satisfy the initially prescribed buoyancy number of geodynamic models by varying iron and/or bridgmanite enrichment (where iron partitioning is depth-dependent following Nakajima et al. (2012)). Each buoyancy number can be fit by a range of compositions given a particular pyrolitic background composition, and the resulting trade-offs between iron enrichment and bridgmanite depletion/enrichment for each buoyancy number are shown in Figure S5 in Supplementary Information. For simulations that have been categorised as 'piles', we calculate the seismic properties of each cell of the simulation output for the range of potential compositions. We use the fraction of compositionally distinct material in each cell to proportion each distinct pile composition and a pyrolitic composition. We include the temperature output from the simulation and add a self-consistent mantle adiabat. To evaluate if a case is seismically 'LLSVP-like', we compute average deviations between the pile and a 1D background model (see Figure S6 in Supplementary Information). We judge a case 'LLSVP-like' if $\mathrm{d}lnV_S$ is lower than -2%, $\mathrm{d}lnV_S/\mathrm{d}lnV_P$ is greater than 1.5 and $\mathrm{d}ln\rho$ is 0.25-1.0%. The density constraint is chosen based on the mean pile density deviation observed in our geodynamic models, but note that we allow for some inconsistency in density between our geodynamic

model and our seismic computations, as the latter is the result of thermo-elastic computations for the considered compositions under high pressure and temperature conditions.

We find that a range of plausible compositions are able to satisfy the criteria for an LLSVP-like appearance (the approved compositional ranges are listed in Table S6 in Supplementary Information), including many cases where internal heating is elevated due to HPE enrichment. Typically the pile cases with a buoyancy number of 0.6 do not produce an LLSVP-like appearance as the pile densities are relatively low and the temperature increase due to HPE enrichment more than offsets the compositional buoyancy. The main exception to this case are the runs with large concentrations of decaying heat production and an initial layer of 150 km, where overturning events redistribute material. Figure 5 shows results for two cases with HPE enrichment of 1x and 20x the background concentration. Pile material for both cases is enriched in iron and slightly depleted in silica compared to the ambient mantle. The compositional buoyancy is offset to different degrees by the thermal buoyancy originating from the internal heating. Where heating is low (equal to the mantle HPE concentration) this results in an excess density which fails our criteria of being comparable to our computational runs. Furthermore, the strength of wave speed reduction in V_S and V_P are too similar compared to seismic observations where V_S is more reduced than V_P. With significantly increased heat production, the excess density of the pile is reduced to close to zero by the thermal buoyancy and both V_S and V_P are more strongly reduced, with a relative stronger reduction for V_S. For this buoyancy number (0.8) we show that our piles can produce seismic properties akin to those of LLSVPs within reasonable compositional limits due to strong enrichment in HPEs. Moreover, if LLSVPs are to be enriched in iron, they may need elevated internal heating budgets to explain the lack of an observable strongly positive density signature. We find that in cases where piles have low concentrations of HPEs, the ratio of $\mathrm{d}lnV_S$ to $\mathrm{d}lnV_P$ approaches unity for low iron enrichment. If LLSVPs are to have larger amplitude in the relative V_S reduction versus V_P, they may be required to be enriched in HPEs and iron to satisfy this ratio as well as density.

4.4 Considerations and Future work

As seen in our regime diagram (Figure 3), the boundary between regimes is not always continuous. For example, for the decay heating case with h=300 km and B=0.6, the 5x HPE simulation has more CMB coverage in the last 500 Myr than both the 1x and 10x HPE simulations, leading to the 5x HPE case being classified in the layer regime while the bordering 1x and 10x HPE cases are classified in the piles regime. Similar behavior is seen in the regime diagram for the constant heating h=150 km case. This is likely due to a degree of randomness present in our simulations. We limit each cell to contain 60-80 tracer particles, which are randomly created and destroyed to meet this restriction after tracers are advected into and out of neighboring cells. The random creation and destruction of tracers is not fully reproducible and can result in slightly varied end states. We expect that using more tracers or running multiple simulations and averaging them would smooth out these discontinuities in the regime diagram. For a few select cases we increased the amount of tracer particles and observed slightly more reproducible behavior, however, it was too computationally expensive to run all of our simulations with more tracers. Additionally, the transition between regimes is progressive, and the discrete boundary values we chose may reside on a transitional regime between layered convection and piles, which may explain some of the erratic boundaries observed in the regime diagram. The regime diagram can thus be viewed as more of a general trend, and artifacts at the boundaries between regimes are likely numerical or reflective of transitional behavior between regimes. In exploratory simulations, we also found that a slightly different initial temperature condition (a longer wavelength perturbation) could also change some of the behavior of the simulations, although the qualitative end state of the simulation remained the same.

More complex models are not expected to significantly alter the general trends we observe in our regime diagram, but may shift the regime diagram or alter pile morphology. In

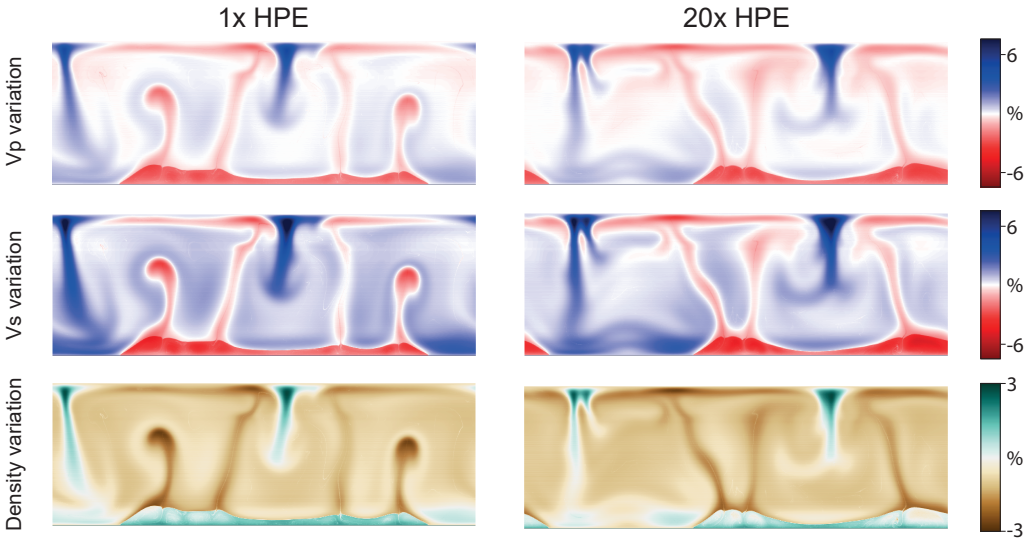

Figure 5: Example cases of calculated dlnV_P (top), dlnV_S (middle) and $d\rho$ (lower) variations from an average 1D model constructed from all pile producing cases with constant heat production. Both simulations have an initial basal layer thickness of 150 km and a buoyancy number of 0.8 and differ in HPE concentration of pile material with 1x (left) and 20x (right). The pile compositions for both cases is strongly enriched in Fe to fit the buoyancy and slightly depleted in Si compared to the ambient mantle: 56% bridgmanite, 37% ferropericlase, 7% Ca-pv, and with 20% iron content (of magnesium bearing minerals). Background mantle composition is 62% bridgmanite, 31% ferropericlase and 7% calcium perovskite with 6.3% iron. Mean seismic contrasts between pile and mantle in these snapshots are -1.52% dlnV_P, -1.84% dlnV_S and 2.23% d$ln\rho$ for the 1x heating case and -2.69% dlnV_P, -4.24% dlnV_S and 0.82% d$ln\rho$ for the 20x heating case. Note that the case on the left is disregarded in our analyses as the computed density contrast is inconsistent with our simulation and the dlnV_S/dlnV_P ratio is too low compared to seismic observations.

particular, 3D cartesian or spherical geometry could affect the flow pattern and accumulation of piles (Deschamps & Tackley, 2008). Spherical geometry would also alter the volume and mass balance of the basal layer relative to the rest of the mantle, affecting the amount of HPE enrichment at which piles are stable for a given layer thickness, and altering the overall thermal evolution of the system and the heat flux from the core. Pile morphology can also be affected by other compositional considerations, such as viscosity. The piles in our simulations are observed to become hot (e.g., Figure 1), which reduces the pile viscosity. Low pile viscosity can result in reduced pile height (Y. Li et al., 2019). It is difficult to decouple the effects of buoyancy versus pile viscosity in our simulations, but it appears that pile viscosity can have an additional effect on pile formation and morphology (Y. Li et al., 2019). A compositional viscosity increase of pile material relative to the background mantle can increase pile stability and increase the height of enriched piles (Y. Li et al., 2019), however, we leave a full exploration of the additional effect of compositional viscosity changes to future work. Increasing the bulk modulus of the piles can also lead to steeper pile topography that is more consistent with seismic observations (Tan et al., 2011). Due to the simplified approximations implemented in our simulations, direct quantitative comparisons with the Earth are difficult.

Our seismic analysis is limited to broad scale seismic signatures. The compositional space only explores enrichment in Si (i.e. higher fraction of bridgmanite vs periclase) and Fe (on the Mg-site in bridgmanite and periclase). Our regime diagram mainly explores

potential theoretical compositions of a primordial layer, which is more consistent with the initial condition of our model. Despite this we find that the seismic attributes of LLSVPs can be produced by piles strongly enriched in HPEs by varying iron and silica content within published estimates. Exploring potential MORB compositions would require testing various specific MORB compositions and Si/Fe enrichment ratios. Recently, it has been suggested that Ca-perovskite in MORB can play a major role in explaining LLSVP velocities (Thomson et al., 2019). This is an interesting scenario for HPE-enriched piles, as aluminous Ca-perovskite is also shown to easily incorporate HPEs (Gautron et al., 2006; Perry et al., 2017). Other suggestions for the composition of LLSVPs include metallic iron (Z. Zhang et al., 2016), hydrous phases (Jiang & Zhang, 2019), and enrichment in both Fe and Al (Fukui et al., 2016). For most of these scenarios there is limited constraint on the resulting densities and seismic velocities in the P-T space required for our study.

5 Conclusions

We find that thermochemical piles at the base of the mantle can form and remain stable even if they are enriched in HPEs by a factor of 5 to 25 times ambient mantle concentrations, given our particular model assumptions. The stability of dense piles enriched in HPEs depends strongly on B, and piles were most stable for $B = 0.6$ and 0.8 (Figure 3), however, these specific numbers may change given a more complex model. The range of possible values of HPE enrichment and B that produce stable piles can be further constrained by the piles' morphological and seismological likeness to LLSVPs. This is achieved within expected compositions for ambient lower mantle and LLSVPs. For certain thermal histories, in particular, decaying heat production (explored for large parameter space compared to previous studies), the available parameter combinations which may satisfy trends of LLSVP seismic behaviour is reduced (Table S1). Our results provide a continuation of the work of Kellogg et al. (1999) and van Thienen et al. (2005) and indicate that dense piles may provide a stable, deep reservoir of primordial material enriched in HPEs. Such a reservoir could provide a possible source of the enriched material found in OIBs, and is compatible with present-day observations of LLSVPs.

Acknowledgments

We thank Ed Garnero and two anonymous reviewers for comments that helped to improve the manuscript, and editor Maureen Long for handling the manuscript. This work began as part of the 2018 Cooperative Institute for Dynamic Earth Research (CIDER) summer program. We thank all organizers and participants of CIDER, which is funded by the National Science Foundation. We owe particular thanks to the other participants of our CIDER group project (SHEEP - Stable HPE-Enriched Provinces) that helped with the initial stages of the project: Jun Yan, Ma Teresa Escobar, and Xiaobao Lin. We also thank Rene Gassmoeller, Rita Parai, Sujoy Mukhopadhyay, Maxim Ballmer, Louise Kellogg, and Michael Manga for helpful discussions. We thank the Computational Infrastructure for Geodynamics (geodynamics.org) which is funded by the NSF under award EAR-0949446 and EAR-1550901 for supporting the development of ASPECT. SC and a meeting for this project have been funded by the European Research Council (ERC) under the European Unions Horizon 2020 research and innovation programme (grant agreement No. 804071 -ZoomDeep). This work used the Savio computational cluster (Berkeley Research Computing, UC Berkeley), resources of the National Energy Research Scientific Computing Center, and the coeus cluster at Portland State University, supported by the NSF Major Research Instrumentation program through DMS-1624776. Support for D. Lourenco was provided through NSF EAR-1622464. The data produced by this study is available on the public repository https://doi.org/10.5281/zenodo.3550321. We dedicate this manuscript to Louise Kellogg.

References

Alzetta, G., Arndt, D., Bangerth, W., Boddu, V., Brands, B., Davydov, D., ... Wells, D. (2018). The `deal.II` library, version 9.0. *Journal of Numerical Mathematics*, *26*(4), 173–183. doi: 10.1515/jnma-2018-0054

Arevalo, R., McDonough, W. F., Stracke, A., Willbold, M., Ireland, T. J., & Walker, R. J. (2013). Simplified mantle architecture and distribution of radiogenic power. *Geochemistry, Geophysics, Geosystems*, *14*(7), 2265-2285. doi: 10.1002/ggge.20152

Ballmer, M. D., Houser, C., Hernlund, J. W., Wentzcovitch, R. M., & Hirose, K. (2017). Persistence of strong silica-enriched domains in the Earths lower mantle. *Nature Geoscience*, *10*(3), 236. doi: 10.1038/ngeo2898

Ballmer, M. D., Lourenço, D. L., Hirose, K., Caracas, R., & Nomura, R. (2017). Reconciling magma-ocean crystallization models with the present-day structure of the Earth's mantle. *Geochemistry, Geophysics, Geosystems*, *18*(7), 2785–2806. doi: 10.1002/2017GC006917

Ballmer, M. D., Schumacher, L., Lekic, V., Thomas, C., & Ito, G. (2016). Compositional layering within the large low shear-wave velocity provinces in the lower mantle. *Geochemistry, Geophysics, Geosystems*, *17*(12), 5056–5077. doi: 10.1002/2016GC006605

Bangerth, W., Dannberg, J., Gassmöller, R., Heister, T., et al. (2018a, may). ASPECT: Advanced Solver for Problems in Earth's ConvecTion, User Manual. doi: 10.6084/m9.figshare.4865333

Bangerth, W., Dannberg, J., Gassmöller, R., Heister, T., et al. (2018b, June). *ASPECT v2.0.1 [software].* Davis, CA. doi: 10.5281/zenodo.1297145

Becker, T. W., Kellogg, J. B., & O'Connell, R. J. (1999). Thermal constraints on the survival of primitive blobs in the lower mantle. *Earth and Planetary Science Letters*, *171*(3), 351–365. doi: 10.1016/S0012-821X(99)00160-0

Buffett, B. (2014). Geomagnetic fluctuations reveal stable stratification at the top of the Earth's core. *Nature*, *507*(7493), 484–487. doi: 10.1038/nature13122

Burke, K., Steinberger, B., Torsvik, T. H., & Smethurst, M. A. (2008). Plume generation zones at the margins of large low shear velocity provinces on the core–mantle boundary. *Earth and Planetary Science Letters*, *265*(1-2), 49–60. doi: 10.1016/j.epsl.2007.09.042

Christensen, U., & Hofmann, A. (1994). Segregation of subducted oceanic crust in the convecting mantle. *Journal of Geophysical Research: Solid Earth*, *99*(93), 19867–19884.

Christensen, U. R. (1985). Thermal evolution models for the earth. *Journal of Geophysical Research: Solid Earth*, *90*(B4), 2995–3007. doi: 10.1029/JB090iB04p02995

Coltice, N., & Ricard, Y. (1999). Geochemical observations and one layer mantle convection. *Earth and Planetary Science Letters*, *174*(1-2), 125–137. doi: 10.1016/S0012-821X(99)00258-7

Conrad, C. P., Steinberger, B., & Torsvik, T. H. (2013). Stability of active mantle upwelling revealed by net characteristics of plate tectonics. *Nature*, *498*(7455), 479–482. doi: 10.1038/nature12203

Cottaar, S., Heister, T., Rose, I., & Unterborn, C. (2014). Burnman: A lower mantle mineral physics toolkit. *Geochemistry, Geophysics, Geosystems*, *15*(4), 1164–1179. doi: 10.1002/2013GC005122

Cottaar, S., & Lekic, V. (2016). Morphology of seismically slow lower-mantle structures. *Geophysical Journal International*, *207*(2), 1122–1136. doi: 10.1093/gji/ggw324

Davaille, A. (1999). Simultaneous generation of hotspots and superwells by convetion in a heterogeneous planetary mantle. *Nature*, *402*(6763), 756–760. doi: 10.1038/45461

Davies, D. R., Goes, S., & Lau, H. C. P. (2015). Thermally dominated deep mantle LLSVPs: a review. In *The Earth's Heterogeneous Mantle* (pp. 441–477). Springer.

Davies, G. F. (1984). Geophysical and isotopic constraints on mantle convection: An interim synthesis. *Journal of Geophysical Research: Solid Earth*, *89*(B7), 6017-6040. doi: 10.1029/JB089iB07p06017

Deschamps, F., Cobden, L., & Tackley, P. J. (2012). The primitive nature of large low shear-wave velocity provinces. *Earth and Planetary Science Letters*, *349*, 198–208.

doi: 10.1016/j.epsl.2012.07.012

Deschamps, F., Kaminski, E., & Tackley, P. J. (2011). A deep mantle origin for the primitive signature of ocean island basalt. *Nature Geoscience*, *4*(12), 879. doi: doi:10.1038/ngeo1295

Deschamps, F., Li, Y., & Tackley, P. J. (2015). Large-scale thermo-chemical structure of the deep mantle: observations and models. In *The Earth's Heterogeneous Mantle: A Geophysical, Geodynamical, and Geochemical Perspective* (pp. 479–515). Cham: Springer International Publishing. doi: 10.1007/978-3-319-15627-9_15

Deschamps, F., & Tackley, P. J. (2008). Searching for models of thermo-chemical convection that explain probabilistic tomography: I. principles and influence of rheological parameters. *Physics of the Earth and Planetary Interiors*, *171*(1-4), 357–373.

Deschamps, F., & Tackley, P. J. (2009). Searching for models of thermo-chemical convection that explain probabilistic tomography. II-Influence of physical and compositional parameters. *Physics of the Earth and Planetary Interiors*, *176*(1-2), 1–18. doi: 10.1016/j.pepi.2009.03.012

Deuss, A., Ritsema, J., & Heijst, H. v. (2011). Splitting function measurements for Earth's longest period normal modes using recent large earthquakes. *Geophysical Research Letters*, *38*(4). Retrieved 2019-07-12, from `https://agupubs.onlinelibrary.wiley.com/doi/abs/10.1029/2010GL046115` doi: 10.1029/2010GL046115

Deuss, A., Ritsema, J., & van Heijst, H. (2013, May). A new catalogue of normal-mode splitting function measurements up to 10 mHz. *Geophysical Journal International*, *193*(2), 920–937. Retrieved 2019-07-12, from `https://academic.oup.com/gji/article/193/2/920/633769` doi: 10.1093/gji/ggt010

Dziewonski, A. M., Lekic, V., & Romanowicz, B. A. (2010). Mantle Anchor Structure: An argument for bottom up tectonics. *Earth and Planetary Science Letters*, *299*(1-2), 69–79. doi: 10.1016/j.epsl.2010.08.013

French, S. W., & Romanowicz, B. (n.d.). Broad plumes rooted at the base of the earth's mantle beneath major hotspots. *Nature*, *525*.

Fukui, H., Yoneda, A., Nakatsuka, A., Tsujino, N., Kamada, S., Ohtani, E., ... Baron, A. Q. R. (2016). Effect of cation substitution on bridgmanite elasticity: A key to interpret seismic anomalies in the lower mantle. *Scientific Reports*, *6*, 33337. doi: 10.1038/srep33337

Garnero, E. J., & McNamara, A. K. (2008). Structure and dynamics of Earth's lower mantle. *Science*, *320*(5876), 626–628. doi: 10.1126/science.1148028

Gassmöller, R., Heien, E., Puckett, E. G., & Bangerth, W. (2016). Flexible and scalable particle-in-cell methods for massively parallel computations. *arXiv preprint arXiv:1612.03369*. Retrieved from `https://arxiv.org/abs/1612.03369`

Gassmöller, R., Lokavarapu, H., Bangerth, W., & Puckett, E. G. (2019). Evaluating the accuracy of hybrid finite element/particle-in-cell methods for modelling incompressible stokes flow. *Geophysical Journal International*, *219*(3), 1915–1938. doi: 10.1093/gji/ggz405

Gautron, L., Greaux, S., Andrault, D., Bolfan-Casanova, N., Guignot, N., & Bouhifd, M. A. (2006). Uranium in the earth's lower mantle. *Geophysical Research Letters*, *33*(23). doi: 10.1029/2006GL027508

Heister, T., Dannberg, J., Gassmöller, R., & Bangerth, W. (2017). High accuracy mantle convection simulation through modern numerical methods. II: Realistic models and problems. *Geophysical Journal International*, *210*(2), 833-851. doi: 10.1093/gji/ggx195

Hernlund, J. W., & Houser, C. (2008). On the statistical distribution of seismic velocities in earth's deep mantle. *Earth and Planetary Science Letters*, *265*(3-4), 423–437.

Hofmann, A. W. (1997). Mantle geochemistry: The message from oceanic volcanism. *Nature*, *385*(6613), 219-229. doi: 10.1038/385219a0

Huang, Y., Chubakov, V., Mantovani, F., Rudnick, R. L., & McDonough, W. F. (2013). A reference Earth model for the heat-producing elements and associated geoneutrino flux. *Geochemistry, Geophysics, Geosystems*, *14*(6), 2003-2029. doi: 10.1002/ggge.20129

Ishii, M., & Tromp, J. (2001, April). Even-degree lateral variations in the Earth's mantle constrained by free oscillations and the free-air gravity anomaly. *Geophysical Journal of the Royal Astronomical Society*, *145*(1), 77–96. doi: 10.1111/j.1365-246X.2001.00385.x

Jackson, J. M., Sinogeikin, S. V., Jacobsen, S. D., Reichmann, H. J., Mackwell, S. J., & Bass, J. D. (2006). Single-crystal elasticity and sound velocities of (Mg0.94Fe0.06)O ferropericlase to 20 GPa. *Journal of Geophysical Research: Solid Earth*, *111*(B9). doi: 10.1029/2005JB004052

Jaupart, C., Labrosse, S., Lucazeau, F., & Mareschal, J. C. (2015). Temperatures, Heat, and Energy in the Mantle of the Earth. In G. Schubert (Ed.), *Treatise on Geophysics (Second Edition)* (p. 223-270). Oxford: Elsevier. doi: 10.1016/B978-0-444-53802-4.00126-3

Javoy, M. (1999). Chemical earth models. *Comptes Rendus de l'Académie des Sciences - Series IIA - Earth and Planetary Science*, *329*(8), 537-555. doi: 10.1016/S1251-8050(00)87210-9

Javoy, M., Kaminski, E., Guyot, F., Andrault, D., Sanloup, C., Moreira, M., ... Jaupart, C. (2010). The chemical composition of the Earth: Enstatite chondrite models. *Earth and Planetary Science Letters*, *293*(3-4), 259-268. doi: 10.1016/j.epsl.2010.02.033

Jiang, J., & Zhang, F. (2019). Theoretical studies on the hydrous lower mantle and D" layer minerals. *Earth and Planetary Science Letters*, *525*, 115753. doi: 10.1016/j.epsl.2019.115753

Kellogg, L. H. (1992). Mixing in the mantle. *Annual Review of Earth and Planetary Sciences*, *20*(1), 365–388. doi: 10.1146/annurev.ea.20.050192.002053

Kellogg, L. H. (1997). Growing the Earth's D" layer: Effect of density variations at the core-mantle boundary. *Geophysical research letters*, *24*(22), 2749–2752. doi: 10.1029/97GL02952

Kellogg, L. H., Hager, B. H., & Van Der Hilst, R. D. (1999). Compositional stratification in the deep mantle. *Science*, *283*(5409), 1881–1884. doi: 10.1126/science.283.5409.1881

Kellogg, L. H., & Wasserburg, G. J. (1990). The role of plumes in mantle helium fluxes. *Earth and Planetary Science Letters*, *99*(3), 276–289. doi: 10.1016/0012-821X(90)90116-F

Koelemeijer, P., Deuss, A., & Ritsema, J. (2017). Density structure of earths lowermost mantle from stoneley mode splitting observations. *Nature Communications*, *8*(1), 1–10. doi: 10.1038/ncomms15241

Koelemeijer, P., Ritsema, J., Deuss, A., & Van Heijst, H.-J. (2015). SP12RTS: a degree-12 model of shear-and compressional-wave velocity for Earth's mantle. *Geophysical Journal International*, *204*(2), 1024–1039. doi: 10.1093/gji/ggv481

Kronbichler, M., Heister, T., & Bangerth, W. (2012). High accuracy mantle convection simulation through modern numerical methods. *Geophysical Journal International*, *191*, 12-29. doi: 10.1111/j.1365-246X.2012.05609.x

Kuo, C., & Romanowicz, B. (2002, July). On the resolution of density anomalies in the Earth's mantle using spectral fitting of normal-mode data. *Geophysical Journal International*, *150*(1), 162–179. Retrieved 2019-07-11, from `https://academic.oup.com/gji/article/150/1/162/591652` doi: 10.1046/j.1365-246X.2002.01698.x

Labrosse, S., Hernlund, J., & Coltice, N. (2007). A crystallizing dense magma ocean at the base of the Earths mantle. *Nature*, *450*(7171), 866. doi: 10.1038/nature06355

Lau, H. C., Mitrovica, J. X., Davis, J. L., Tromp, J., Yang, H.-Y., & Al-Attar, D. (2017). Tidal tomography constrains Earths deep-mantle buoyancy. *Nature*, *551*(7680), 321. doi: 10.1038/nature24452

Lay, T., & Garnero, E. J. (2011). Deep mantle seismic modeling and imaging. *Annual Review of Earth and Planetary Sciences*, *39*, 91–123. doi: 10.1146/annurev-earth-040610-133354

Le Bars, M., & Davaille, A. (2004). Whole layer convection in a heterogeneous planetary mantle. *Journal of Geophysical Research*, *109*(B3), B03403. doi: 10.1029/2003JB002617

Lekic, V., Cottaar, S., Dziewonski, A., & Romanowicz, B. (2012). Cluster analysis of global lower mantle tomography: A new class of structure and implications for chemical heterogeneity. *Earth and Planetary Science Letters*, *357*, 68–77. doi: 10.1016/j.epsl.2012.09.014

Li, M., & McNamara, A. K. (2018). The influence of deep mantle compositional heterogeneity on Earth's thermal evolution. *Earth and Planetary Science Letters*, *500*, 86–96. doi: 10.1016/j.epsl.2018.08.009

Li, M., McNamara, A. K., & Garnero, E. J. (2014). Chemical complexity of hotspots caused by cycling oceanic crust through mantle reservoirs. *Nature Geoscience*, *7*(5), 366. doi: 10.1038/ngeo2120

Li, M., Zhong, S., & Olson, P. (2018). Linking lowermost mantle structure, core-mantle boundary heat flux and mantle plume formation. *Physics of the Earth and Planetary Interiors*, *277*(December 2017), 10–29. doi: 10.1016/j.pepi.2018.01.010

Li, Y., Deschamps, F., Yang, J., Chen, L., Zhao, L., & Tackley, P. J. (2019, aug). Effects of the Compositional Viscosity Ratio on the LongTerm Evolution of Thermochemical Reservoirs in the Deep Mantle. *Geophysical Research Letters*, *46*(16), 9591–9601. doi: 10.1029/2019gl083668

Limare, A., Jaupart, C., Kaminski, E., Fourel, L., & Farnetani, C. G. (2019). Convection in an internally heated stratified heterogeneous reservoir. *Journal of Fluid Mechanics*, *870*, 67–105. doi: 10.1017/jfm.2019.243

Mao, Z., Jacobsen, S., Jiang, F., Smyth, J., Holl, C., Frost, D., & Duffy, T. S. (2008). Single-crystal elasticity of wadsleyites, β-Mg2SiO4, containing 0.37–1.66 wt.% H2O. *Earth and Planetary Science Letters*, *266*(1-2), 78–89. doi: 10.1016/j.epsl.2007.10.045

McDonough, W., & Sun, S.-s. (1995). The composition of the Earth. *Chemical Geology*, *120*(3-4), 223-253. doi: 10.1016/0009-2541(94)00140-4

McNamara, A. K. (2019). A review of large low shear velocity provinces and ultra low velocity zones. *Tectonophysics*, *760*, 199–220. doi: 10.1016/j.tecto.2018.04.015

McNamara, A. K., & Van Keken, P. E. (2000). Cooling of the Earth: A parameterized convection study of whole versus layered models. *Geochemistry, Geophysics, Geosystems*, *1*(11). doi: 10.1029/2000GC000045

McNamara, A. K., & Zhong, S. (2004). Thermochemical structures within a spherical mantle: Superplumes or piles? *Journal of Geophysical Research: Solid Earth*, *109*(B7). doi: 10.1029/2003JB002847

McNamara, A. K., & Zhong, S. (2005). Thermochemical structures beneath Africa and the Pacific Ocean. *Nature*, *437*(7062), 1136. doi: 10.1038/nature04066

Montague, N. L., & Kellogg, L. H. (2000). Numerical models of a dense layer at the base of the mantle and implications for the geodynamics of D". *Journal of Geophysical Research: Solid Earth*, *105*(B5), 11101–11114. doi: 10.1029/1999JB900450

Moulik, P., & Ekström, G. (2016). The relationships between large-scale variations in shear velocity, density, and compressional velocity in the Earth's mantle. *Journal of Geophysical Research: Solid Earth*, *121*(4), 2737–2771. doi: 10.1002/2015JB012679

Mukhopadhyay, S. (2012). Early differentiation and volatile accretion recorded in deep-mantle neon and xenon. *Nature*, *486*(7401), 101. doi: 10.1038/nature11141

Mulyukova, E., Steinberger, B., Dabrowski, M., & Sobolev, S. V. (2015). Survival of LLSVPs for billions of years in a vigorously convecting mantle: replenishment and destruction of chemical anomaly. *Journal of Geophysical Research: Solid Earth*, *120*(5), 3824–3847. doi: 10.1002/2014JB011688

Nakagawa, T., & Tackley, P. J. (2004). Effects of thermo-chemical mantle convection on the thermal evolution of the Earths core. *Earth and Planetary Science Letters*, *220*(1-2), 107–119. doi: 10.1016/S0012-821X(04)00055-X

Nakagawa, T., & Tackley, P. J. (2014). Influence of combined primordial layering and recycled morb on the coupled thermal evolution of earth's mantle and core. *Geochemistry, Geophysics, Geosystems*, *15*(3), 619–633. doi: 10.1002/2013GC005128

Nakajima, Y., Frost, D. J., & Rubie, D. C. (2012). Ferrous iron partitioning between magnesium silicate perovskite and ferropericlase and the composition of perovskite in

the Earth's lower mantle. *Journal of Geophysical Research: Solid Earth*, *117*(B8). doi: 10.1029/2012JB009151

Ni, S., & Helmberger, D. V. (2003). Ridge-like lower mantle structure beneath south africa. *Journal of Geophysical Research: Solid Earth*, *108*(B2). doi: 10.1029/2001JB001545

O'Neill, H. S., & Palme, H. (2008). Collisional erosion and the non-chondritic composition of the terrestrial planets. *Philosophical Transactions of the Royal Society A: Mathematical, Physical and Engineering Sciences*, *366*(1883), 4205-4238. doi: 10.1098/rsta.2008.0111

Palme, H., & O'Neill, H. (2014). Cosmochemical Estimates of Mantle Composition. In *Treatise on Geochemistry* (p. 1-39). Elsevier. doi: 10.1016/B978-0-08-095975-7.00201-1

Perry, S. N., Pigott, J. S., & Panero, W. R. (2017). Ab initio calculations of uranium and thorium storage in casio3-perovskite in the earths lower mantle. *American Mineralogist*, *102*(2), 321–326. doi: 10.2138/am-2017-5816

Pető, M. K., Mukhopadhyay, S., & Kelley, K. A. (2013). Heterogeneities from the first 100 million years recorded in deep mantle noble gases from the Northern Lau Back-arc Basin. *Earth and Planetary Science Letters*, *369*, 13–23. doi: 10.1016/j.epsl.2013.02.012

Resovsky, J. S., & Ritzwoller, M. H. (1995). Constraining odd-degree earth structure with coupled free-oscillations. *Geophysical Research Letters*, 2301–2304. Retrieved 2019-07-25, from `https://agupubs.onlinelibrary.wiley.com/doi/abs/10.1029/95GL01996%4010.1002/%28ISSN%291944-8007.BOLIVEQ1` doi: 10.1029/95GL01996@10.1002/(ISSN)1944-8007.BOLIVEQ1

Rudnick, R., & Gao, S. (2014). Composition of the Continental Crust. In *Treatise on Geochemistry* (p. 1-51). Elsevier. doi: 10.1016/B978-0-08-095975-7.00301-6

Ruedas, T. (2017). Radioactive heat production of six geologically important nuclides. *Geochemistry, Geophysics, Geosystems*, *18*(9), 3530-3541. doi: 10.1002/2017GC006997

Šrámek, O., McDonough, W. F., Kite, E. S., Lekić, V., Dye, S. T., & Zhong, S. (2013). Geophysical and geochemical constraints on geoneutrino fluxes from Earth's mantle. *Earth and Planetary Science Letters*, *361*, 356-366. doi: 10.1016/j.epsl.2012.11.001

Stixrude, L., & Lithgow-Bertelloni, C. (2011). Thermodynamics of mantle minerals-II. Phase equilibria. *Geophysical Journal International*, *184*(3), 1180–1213. doi: 10.1111/j.1365-246X.2010.04890.x

Tackley, P. J. (1998). Three-dimensional simulations of mantle convection with a thermochemical basal boundary layer: D"? *The Core-Mantle Boundary Region*, *28*, 231–253.

Tackley, P. J. (2011). Living dead slabs in 3-D: The dynamics of compositionally-stratified slabs entering a slab graveyard above the core-mantle boundary. *Physics of the Earth and Planetary Interiors*, *188*(3-4), 150–162. doi: 10.1016/j.pepi.2011.04.013

Tan, E., Leng, W., Zhong, S., & Gurnis, M. (2011, jul). On the location of plumes and lateral movement of thermochemical structures with high bulk modulus in the 3-D compressible mantle. *Geochemistry, Geophysics, Geosystems*, *12*(7), n/a–n/a. doi: 10.1029/2011GC003665

Tesoniero, A., Cammarano, F., & Boschi, L. (2016). S- to- P heterogeneity ratio in the lower mantle and thermo-chemical implications. *Geochemistry, Geophysics, Geosystems*, *17*(7), 2522–2538. doi: 10.1002/2016GC006293

Thomson, A., Crichton, W., Brodholt, J., Wood, I., Siersch, N., Muir, J., ... Hunt, S. (2019). Seismic velocities of CaSiO3 perovskite can explain LLSVPs in Earths lower mantle. *Nature*, 1–5. doi: 10.5285/6db95d87-365f-4018-abec-00e96e8fcf8d

To, A., Romanowicz, B., Capdeville, Y., & Takeuchi, N. (2005). 3D effects of sharp boundaries at the borders of the African and Pacific Superplumes: Observation and modeling. *Earth and Planetary Science Letters*, *233*(1-2), 137–153. doi: 10.1016/j.epsl.2005.01.037

Tolstikhin, I., Kramers, J. D., & Hofmann, A. (2006). A chemical Earth model with whole mantle convection: the importance of a core–mantle boundary layer (D") and its early formation. *Chemical Geology*, *226*(3-4), 79–99. doi: 10.1016/j.chemgeo.2005.09.015

Turcotte, D. L., & Schubert, G. (2014). *Geodynamics*. Cambridge University Press.

van Summeren, J., Van den Berg, A., & Van der Hilst, R. (2009). Upwellings from a deep mantle reservoir filtered at the 660 km phase transition in thermo-chemical convection models and implications for intra-plate volcanism. *Physics of the Earth and Planetary Interiors*, *172*(3-4), 210–224. doi: 10.1016/j.pepi.2008.09.011

van Thienen, P., van Summeren, J., van der Hilst, R. D., van den Berg, A. P., & Vlaar, N. J. (2005). Numerical study of the origin and stability of chemically distinct reservoirs deep in Earths mantle. *Geophysical Monograph*. doi: 10.1029/160GM09

Wang, Y., & Wen, L. (2007). Geometry and p and s velocity structure of the african anomaly. *Journal of Geophysical Research: Solid Earth*, *112*(B5). doi: 10.1029/2006JB004483

White, W. M. (2015). Isotopes, DUPAL, LLSVPs, and Anekantavada. *Chemical Geology*, *419*, 10-28. doi: 10.1016/j.chemgeo.2015.09.026

Woodhead, J., Hergt, J., Giuliani, A., Maas, R., Phillips, D., Pearson, D. G., & Nowell, G. (2019). Kimberlites reveal 2.5-billion-year evolution of a deep, isolated mantle reservoir. *Nature*, *573*(7775), 578–581. doi: 10.1038/s41586-019-1574-8

Zhang, N., Zhong, S., Leng, W., & Li, Z. X. (2010). A model for the evolution of the Earth's mantle structure since the Early Paleozoic. *Journal of Geophysical Research: Solid Earth*, *115*(6), 1–22. doi: 10.1029/2009JB006896

Zhang, Z., Dorfman, S. M., Labidi, J., Zhang, S., Li, M., Manga, M., ... Williams, Q. (2016). Primordial metallic melt in the deep mantle. *Geophysical Research Letters*, *43*(8), 3693–3699. doi: 10.1002/2016GL068560

References from Supplementary Information:

Fiquet, G., Auzende, A., Siebert, J., Corgne, A., Bureau, H., Ozawa, H., Garbarino, G. (2010). Melting of peridotite to 140 gigapascals. Science, 329 (5998), 15161518. doi: 10.1126/science.1192448

Frost, D. J., Liebske, C., Langenhorst, F., McCammon, C. A., Trnnes, R. G., Rubie, D. C. (2004). Experimental evidence for the existence of iron-rich metal in the Earths lower mantle. Nature, 428 (6981), 409. doi: 10.1038/nature02413